Effect of welding energy on microstructure and strength of ultrasonic spot welded dissimilar joints of aluminum to steel sheets

F.A. Mirza [a], A. Macwan [b], S.D. Bhole [b], D.L. Chen [b,*] and X.-G. Chen [a,*]

[a] *Department of Applied Sciences, University of Québec at Chicoutimi*
555, boulevard de l'Université, Chicoutimi, QC G7H 2B1, Canada

[b] *Department of Mechanical and Industrial Engineering, Ryerson University,*
350 Victoria Street, Toronto, Ontario M5B 2K3, Canada

Abstract

Two dissimilar ultrasonic spot welded joints of aluminum to commercial steel sheets at different levels of welding energy were investigated. The tensile lap shear tests were conducted to evaluate the failure strength in relation to microstructural changes. The main intermetallics at the weld interface in both joints was θ ($FeAl_3$), along with η (Fe_2Al_5) phase in Al-to-AISI 304 stainless steel joint and Fe_3Al phase in Al-to-ASTM A36 steel joint, respectively. The welding strength of Al-to-AISI 304 stainless steel weld samples was slightly higher than Al-to-ASTM A36 steel weld samples, whereas the fracture energies of Al-to-AISI 304 stainless steel weld samples were significantly higher as compared with Al-to-ASTM A36 steel weld samples. The welding strength of both Al-to-Steel welds were higher than other reported dissimilar USW joints in literature. The fracture surfaces of both weld joints exhibits the growth of IMC layer

---

[*] Corresponding authors – X.-G. Chen, Tel: (418) 545-5011 ext. 2603; Fax: (418) 545-5012; Email: xgrant.chen@uqac.ca and D.L. Chen, Tel: (416) 979-5000 ext. 6487; Fax: (416) 979-5265; Email: dchen@ryerson.ca.

with increasing welding energy or time, whose inherent brittleness compromises the integrity of joints. In both cases, the lap shear tensile fracture occurred from the Al/Fe interface at lower energy inputs and the failure mode at higher welding energy inputs became the "transverse through-thickness crack growth" at the edge of the nugget zone on the softer Al side.

Keywords: Dissimilar ultrasonic spot welding; Tensile lap shear strength; Aluminum alloy; Steel alloy; Intermetallic compounds; Tensile fracture.

1. Introduction

Due to the mounting environmental concern to diminish anthropogenic climate-changing, environment-damaging, costly and human death-causing[1] emissions and the ensuing stringent fuel economy regulations in recent years, lightweighting in vehicles has turned into a crucial approach in the automotive and aerospace industries [1-5]. To manufacture lightweight vehicles, advanced high-strength steels, aluminum (Al) alloys, magnesium alloys, and composite materials are being increasingly used in the automotive and aerospace sectors. The applications of Al alloys have been significantly increased in the fabrication of the vehicles because of their high strength-to-weight ratio, good machinability, environmental friendliness and recyclability [6-8]. To expand the use of Al alloys in automotive body manufacturing, lower-cost joining methods are important especially with dissimilar joining capability [8]. In the steel auto body manufacturing, resistance spot welding (RSW) is one of the predominant processes [8,9]. However, RSW consumes high energy and requires frequent electrode maintenance [9]. Furthermore, it is difficult to weld Al alloys by RSW due to their high thermal conductivity [10]. Recently, two solid-state welding processes, i.e., friction stir spot welding (FSSW) [11-13] and ultrasonic spot welding (USW) [6,14-16] are being considered as possible replacement techniques for RSW especially for dissimilar welding. Welding aluminum alloys using a USW process consumes less welding energy (~0.3 kWh per 1000 joints) compared with RSW (20 kWh), and FSSW (2 kWh) [8,17-19]. In addition, unlike RSW and laser welding, a peak temperature during USW does not exceed the melting point of the metal workpiece, eliminating the formation of undesirable compounds, phases and metallurgical defects that commonly observed in most other fusion welds [20,21]. USW technique induces the rubbing of two metal sheets by

---

[1] According to Science News entitled "Air pollution kills 7 million people a year" on March 25, 2014 at http://news.sciencemag.org/signal-noise/2014/03/air-pollution-kills-7-million-people-year: "Air pollution isn't just harming Earth; it's hurting us, too."

maintaining the solid state without melting, which leads to the breaking of oxide layers between contacting surfaces, producing localized heat to soften the material at the weld interface, and eventually resulting in local adhesion and formation of microwelds [18,22]. It is considered as an emerging and promising technique for joining non-ferrous metals and alloys with relatively a lower melting point as well as welding dissimilar material combinations as diverse as metal/ceramic, metal/glass, Al/Cu, and Al/steel [23-26].

Some important factors have to be taken under consideration such as the operating cost, cycle time, reliability, and weld quality to able to successfully join dissimilar metals [6,19,27]. One of the most critical issues during USW is to control the intermetallic compounds (IMCs) that form at the weld interface via a rapid diffusion process [6,8,19,24,27]. It is reported that IMCs are brittle and a continuous IMC interface layer severely compromises the joints strength [6]. To date, most of the studies involving IMC reaction kinetics in Al-Steel couples have been focused on the growth rate of continuous IMC layers developed after long welding times or extended isothermal treatments [28-31]. It is therefore important to thoroughly investigate the formation of IMCs at short weld durations such as in USW of typical commercial alloys for automotive applications. In addition, to minimize the formation of IMCs during the welding, Chen *et al.* [32] used Ni foil as an interlayer in laser penetration welding of Al and steel alloys. Watanabe *et al.* [27] used commercially pure Al sheet A1050-24H as an insert metal in the USW of Al-to-mild steel to study the effect of insert metal on the joint properties. Haddadi *et al.* [24] used Zn-coated steel in USW to minimize the reaction between Al and Fe during the welding. It is also known that in dissimilar welding, the composition of the weld members can strongly affect IMCs formation at the joint interface [28,33], although the relationship to many common alloy additions still remains poorly understood. To the authors' knowledge, there are no systematic studies on the effect of alloy compositions on the formation of IMCs and the consequent mechanical performance of the USW dissimilar welds in the open literature. The present study was, therefore, aimed to gain a better understanding of the influence of IMC formation on the USWed dissimilar Al-to-steel joints. To produce high-integrity joints by USW of aluminum to steel, two typical commercial steel alloys have been used in the current investigation with a particular emphasis on the weld microstructure evolution and mechanical properties.

2. Materials and Experimental Procedure

The materials selected in this investigation were commercially available 1.5 mm thick sheets of Al 6061-T6 alloy and two steel alloys (AISI 304 stainless steel and ASTM A36 steel). The nominal chemical compositions of test materials used are given in Table 1. The specimens, being 60 mm long and 15 mm wide, were sheared, and prior to welding the sheet surfaces were ground with 120-grit sand paper. Then the samples were cleaned in acetone and dried. The welds were produced with a Sonobond dual-head spot welding system at the center of a 20 mm overlap. The welding system was operated at 20 kHz and the joints were produced using an energy input ranging from 250 to 1750 J, a nominal applied power of 2 kW with an impedance setting of 8 and a clamping pressure of 0.4 MPa.

Microstructure examinations was performed using an optical microscope (OM) and scanning electron microscope (SEM, JEOL JSM-6480LV) equipped with energy dispersive X-ray spectroscopy (EDS) electron backscatter diffraction (EBSD) systems. The metallographic samples were cut from the weld cross-section, and then sample preparation was accomplished by standard metallographic technique. A computerized Buehler hardness testing machine was used to determine Vickers microhardness, which was measured diagonally across the joints using a load of 100 g and a 15 s dwell time except for the thin interface layer (10-200 μm), where a load of 10 g was used for 15 s. To evaluate the joint strength, tensile lap shear tests were performed for each welding condition using a fully computerized United testing machine. A 5 kN load cell was used under a constant crosshead speed of 1 mm/min in air at room temperature to avoid the unnecessary dynamic effects. At least two samples were tested at each energy level, however, due to the experimental scatter at certain energy levels i.e., 500 J, 750 J, and 1500 J, three samples were tested. To prevent the rotation and bending moment of specimens during the tensile lap shear tests, two spacers with a thickness of 1.5 mm, width of 15 mm and length of 35 mm were attached at both ends of the specimen. Phase identification on both matching surfaces of Al and steel sides after tensile shear tests was determined using a PANalytical X-ray diffractometer (XRD) with Cu K_α radiation at 45 kV and 40 mA in a back reflection mode. The diffraction angle (2θ) at which the X-rays hit the samples varied from 20 to 100°, with a step size of 0.05° and 2 s in each step. The fracture surfaces were examined via a scanning electron microscope (SEM).

3. Results and Discussion

3.1 Microstructure evolution

To investigate the relationship between physical weld attributes and weld performance, microstructural characterization was conducted on the cross-section of selected welded samples at various welding energy values (500 to 1500 J). Fig. 1 and Fig. 2 show the typical optical micrographs of dissimilar USWed Al-to-AISI 304 stainless steel and Al-to-ASTM A36 steel joint at different welding energy levels. It can be seen from Figs. 1(a) and 2(a) that there exist gaps along the weld interface which show the lack of bonding at a lower energy of 500 J. As the welding energy increases, the gaps at the weld interface become less distinct, which indicates that by increasing weld energy almost sound joints were achieved (Figs. 1(b) and (c) and Figs. 2(b) and (c)). It is more obvious from the magnified images of different regions (indicated by the yellow dashed boxes) of welded joints at different energy levels as shown in Figs. 1(d), (e), and (f) and Figs. 2(d), (e), and (f). For instance, at the highest energy levels (i.e., 1000 J for Al-to-AISI 304 stainless steel and 1500 J for Al-to-ASTM A36 steel joints, respectively), the weld interface does not exhibit any gap (Fig. 1(f) and Fig. 2(f)). However, as compared to Al-to-ASTM A36 steel joints (Fig. 2(f)) (where a clear continuous line mark can be seen at the weld interface indicated by arrow), the weld characteristics of Al-to-AISI 304 stainless steel joints displayed improved bonding (Fig. 1(f)). Furthermore, to observe the weld attributes more diligently, higher magnification SEM back-scattered electron images at the interface of welded joints at different energy inputs are shown in Fig. 3. As seen from Fig. 3, most of the welding conditions showed good bonding since there were no large defects, such as significant crack, void or tunnel type defects, except for the lower energy joints, i.e., 500 J (Figs. 3(a) and (b)). As mentioned before, it is evident from SEM images (Figs. 3(e) and (f)) that sound joints were achieved by increasing welding energy. Furthermore, it is seen from Figs. 1(e), 1(f), 2(e) and 2(f) that interface bonding also occurred via mechanical interlocking due to the solid-state deformation at a higher welding energy levels of 750 J to 1500 J as well as the formation and progressive spreading of microwelds, which would be anticipated to give a high bonding strength. This is associated with a considerable rise in temperature in the weld zone, which softens the material and allows the sonotrode tips to sink into the sheet surfaces. In the process, the weld interface is displaced into complex wave-like flow patterns as indicated by the yellow dashed circles (Figs. 1(e), 1(f), 2(e), and 2(f)). Similar phenomenon was also reported in Refs. [14,17, 19,24,34].

3.2 Energy-dispersive X-ray spectroscopy (EDS) analysis

To verify the chemical composition and possible phases formed during USW, EDS line scan analysis was performed at weld interfaces of Al-to-AISI 304 stainless steel and Al-to-ASTM A36 steel joints at a welding energy of 500 J as shown in Fig. 4. It is seen that the interface composition and microstructure in both joining conditions are not exactly the same i.e., a relatively larger interface diffusion layer formed in Al-to-ASTM A36 steel as compared with Al-to-AISI 304 stainless steel at the same magnification. Previous studies suggested that this layer could be the IMCs containing Al and Fe and these IMCs form along the bonding line of welds through interdiffusion [6,35]. Generally, due to the relatively low melting temperature, Al atoms diffused into Fe lattice in the form of solid solution because they are much more energetic or active during USW [17,36]. As can be seen in the EDS line scan (Figs. 4(a) and (b)) for Al-to-AISI 304 stainless steel, at a distance of ~11 μm the concentration of Al was starting to decrease and then suddenly spiked at a distance of ~15 μm and then again decreased. The scan results clearly show a higher amount of Fe merged with Al at a distance of ~12 μm, then decreased, and a relatively strong Cr element was also present in this particular region. According to the binary phase diagram of Al and Fe, Al has a fairly high solubility in Fe and it can form disordered solid solution in Fe up to ~11 wt.% of alloying [37,38]. Beyond this critical amount of Al, some brittle IMCs such as θ ($FeAl_3$), η (Fe_2Al_5), $FeAl_2$, and FeAl would emerge [6,17,24,35], which were later confirmed by the XRD analysis. Many studies have also reported the presence of these IMC phases during the welding of Al and steel, which is the main cause of fracture [6,35]. Similar results can be seen from Figs. 4(c) and (d) for Al-to-ASTM A36 steel, decreasing the concentration of Al and merged with Fe element, which also suggests forming the IMCs layers of Al and Fe.

3.3 X-ray diffraction analysis and EBSD phase identification

Fig. 5 shows the X-ray diffraction patterns obtained on both matching fracture surfaces of Al and steel sides for both USWed Al-to-AISI 304 stainless steel and Al-to-ASTM A36 steel joints after the tensile lap shear test. It is clear that, apart from strong peaks of Al (Fig. 5(a)) for Al-to-AISI 304 stainless steel joints, peaks of θ ($FeAl_3$), η (Fe_2Al_5) and Cr appeared on both sides of the fracture surfaces. As reported earlier, many studies have reported the presence of θ ($FeAl_3$) and η (Fe_2Al_5) brittle phases during the welding of Al-to-steel [27,32,39-42] even in the USW joints [6,8,17,35,43]. The first phase that forms during metal-to-metal interaction is the phase with the most negative heat of formation at the concentration of the lowest eutectic in the binary system [6]. It was reported that θ ($FeAl_3$) has the largest negative free Gibbs energy of formation and kinetically favored [43]. In the later stage, θ ($FeAl_3$) and Fe phases will react with each other to form a phase with a composition between that of the interacting phases and closest to that of the lowest eutectic composition, i.e., η (Fe_2Al_5), $FeAl_2$, FeAl, and Fe_3Al [33,42,44,45]. This is in agreement with the results presented here as shown in Fig. 5(a). On the other hand, for Al-to-ASTM A36 steel joints (Fig. 5(b)), peaks of θ ($FeAl_3$), Fe_3Al and Fe appeared on both sides of the fracture surfaces apart from the strongest peaks of Al. The main difference between Al-to-AISI 304 stainless steel and Al-to-ASTM A36 steel joints is that, in addition to the common θ ($FeAl_3$) phase in both joints, the Al-to-AISI 304 stainless steel joint contained η (Fe_2Al_5) phase while the Al-to-ASTM A36 steel joint had Fe_3Al phase. The presence of Fe_3Al was also confirmed in laser beam lap joints of A6111-T4-to-cold-rolled steel plates (SPCC) by Lee *et al.* [46]. To further confirm the IMCs formed during USW, EBSD phase identification was also performed in both dissimilar joints (Figs. 6 and 7). The simulation results calculated from the indexed experimental EBSD patterns (Figs. 6(b) and 7(b)) were able to confirm the presence of the $FeAl_3$ in Al-to-AISI 304 stainless steel joint and the Fe_3Al in Al-to-ASTM A36 steel joint. In the EBSD analysis, for an accurate solution, the mean angular deviation (MAD) value must be lower than 0.7 [47,48]. As illustrated in both figures, the MAD value is lower than 0.7, which validates the results of the phase identification obtained for both $FeAl_3$ and Fe_3Al phases.

3.4 Microhardness

Microhardness profiles across the interfaces of dissimilar USWed Al-to-AISI 304 stainless steel and Al-to-ASTM A36 steel joints at different levels of welding energy are shown in Fig. 8. No noticeable heat-affected zone (HAZ) was observed during USW of both joints. It has been reported that, in contrast to other joining methods such as RSW, USW does not exhibit any clearly discernible HAZ that can degrade the strength of the joints as reported by others [6,49]. Obvious asymmetrical type hardness profiles across the both dissimilar joints were obtained with an average hardness value of ~47 HV on the Al 6061-T6 side, ~201 HV on the AISI 304 stainless steel side and ~129 HV on the ASTM A36 steel side. In general, the hardness supposed to decrease with increasing welding energy due to increasing grain size with increasing temperature [15,18,50]. As seen from Fig. 8, only the hardness values in Fe side of ASTM A36 exhibits the decreasing phenomena, whereas it was not obvious in AISI 304 Fe side. However, as compared to the ASTM A36 steel, a significantly higher hardness in AISI 304 stainless steel side was observed, which is due to the solid solution strengthening of Cr and high strength of the bulk AISI 304 stainless steel.

3.5 Joint performance: Lap shear tensile testing and failure mode

The maximum tensile lap shear strengths of dissimilar USWed Al-to-AISI 304 stainless steel and ASTM A36 steel joints as a function of welding energy are shown in Fig. 9. The strength profiles for both joints showed a similar pattern, in which the lap shear strength increased with increasing energy input up to a peak value, then decreased with a further increase in the welding energy or welding time. In comparison with the lap shear strengths, the fracture energy of welded joints exhibited a larger scatter (Fig. 10), however showed a similar trend. The optimum welding energy resulted in a peak value of the fracture energy followed by a decrease. It can be seen that the Al-to-AISI 304 stainless steel welds produced at a welding energy of 750 J (in a welding time of 0.375 s) gave a peak strength of ~87 MPa (~3.5 kN), which is higher than other dissimilar USW joints (with a similar clamping pressure), i.e., a maximum lap shear strength of 3.2 kN for aluminum AA6111-to-DC04 steel joints by Xu *et al.* [35], 2.7 kN for aluminum 6111-T4-to hard zinc-coated DX56-Z steel joints by Haddadi *et al.* [43], 3.1 kN for Al6111-to-hot-dipped Zn-coated steel, and 2.7 kN for Al6111-to-galvanized annealed steel by Haddadi *et al.*

[24] and 0.6 kN for A5052 Al alloy-to-SS400 mild steel by Watanabe *et al.* [27]. Compared to the Al-to-AISI 304 stainless steel welds, the Al-to-ASTM A36 steel welds showed a slightly lower peak strength of ~83 MPa (~3.3 kN) in twice the time (in a 0.75 s welding time) and twice the energy (1500 J) in the lap shear tests and a much lower fracture energy (half of the Al-to-AISI 304 stainless steel weld samples). This difference is clearly associated with the IMCs seen in the Al-to-AISI 304 stainless steel weld samples (as shown in Fig. 5) and also higher hardness value (as shown in Fig. 8). In addition, for the dissimilar joints the current USW process can also be compared with other spot welding [11], for instance, Fukumoto *et al.* [51] obtained a 3.5 kN lap shear strength with a longer welding time of 5 s using friction stir spot welding. Thus, the current results indicate that USW offers a very promising solution for dissimilar metal joining.

It has been established that at lower energy inputs, the temperature was not high enough to soften the sample thereby diffuse the Al into steel to achieve a sound joint [6], which is also verified by microstructure observation in the present study (Fig. 1 to Fig. 3). Fig. 11 shows the effect of welding energy on the tensile lap shear peak load of dissimilar USWed Al-to-AISI 304 stainless steel and Al-to-ASTM A36 steel joints along with typical tensile failure modes and locations. It is observed that in the case of lower energy inputs (e.g., 250 J and 500 J for Al-to-AISI 304 stainless steel joints (Fig. 11(a)) and from 500 J and 750 J for Al-to-ASTM A36 steel joints (Fig. 11(b)), the lap shear tensile fracture occurred from the Al/Fe interface. In the case of Al-to-ASTM A36 steel joints, by increasing the weld energy up to 1250 J, the failure mode was still interfacial; however, the initiation of the crack started at the circumference around the nugget on softer Al side (Fig. 11 (b)). At higher energy inputs (1500 J), the lap shear tensile strength increased with increasing energy inputs due to high temperatures and strain rate under larger vibration amplitude for a longer time, which leads to increased diffusion between Al and

Fe. It was also verified by Haddadi *et al.* [43] that with increasing welding time, i.e., increasing welding energy in the present study, the thickness of the IMCs increased. After achieving the peak strength, as these IMC phases (θ ($FeAl_3$), η (Fe_2Al_5) and Fe_3Al, Fig. 4 and Fig. 5) grew, their inherent low ductility compromised the integrity of the joint. To justify the increase of IMC thickness, Fig. 12 shows some typical SEM back-scattered electron images of tensile fracture surfaces of USWed Al-to-AISI 304 stainless steel and Al-to-ASTM A36 steel joints at different energy inputs. Despite the rapid weld cycle and solid-state nature of the USW process, the fracture surfaces in Fig. 12 indicate that the IMC layer grows with increasing welding energy or time. With lower welding energies (i.e., 250 J and 500 J for AISI 304 and ASTM A36 steel joints, respectively) local areas of contacting asperities on the two sheet surfaces lead to the local formation of IMCs islands where microbonds first form (Fig. 12(a) and (c)), as also reported by Haddadi [43]. The IMC layer was observed to grow with higher welding energies which led to greater fraction of IMC coverage area of the sheet surface (Fig. 12(b) and (d)). As the IMC coverage area is greater during higher welding energies, there is more possibility that failure takes place through the greater brittle Al-Fe interfacial layer observed in Fig. 12, which also suggested that the base material locally reached its fracture strength and the fracture initiated in that area. In addition, as shown in Fig. 5, IMC phases were present on both Al and steel sides of the tensile failed samples, indicating a mode of cohesive failure within an IMC layer. This suggests that failure occurred through the IMC layer due to their inherent brittleness. Indeed, Al present on both sides (Fig. 5) also revealed a cohesive failure within Al base metal at a region where prominent bonding mechanism is mechanical interlocking. Similar observations were also reported by Macwan and Chen [52,53].

It was also reported that during dissimilar USW, there is a competition between the formation and spread of microwelds across the joint interface, which leads to an increasing bonding strength, and the coalescence and thickening of the IMC reaction layer, which eventually encourage a brittle interface failure [35]. In addition, as reported in Refs. [6,15,18,50], the failure mode at higher welding energy levels can be referred to as the "transverse through-thickness crack growth", which occurred at the edge of the nugget zone on the softer Al side, unlike interfacial fracture which occurred at lower energy inputs. Basically, this transverse through-thickness crack growth mode occurred at the edge of the sonotrode in the transverse direction (i.e., perpendicular to the tensile loading) in contact with the sample, which also indicate that the bonding between the two sheets are very good at this energy level since the nugget zone is completely inseparable (as indicated by arrow in higher magnification in Fig. 11). At a further higher welding energy level, the softer Al sheet (due to high temperatures) experiences significant amount of bending at the nugget edge due to the outward flow of the material under the sonotrode tool indentation [6]. This leads to creating a small micro-level crack tip at the notch of two welded sheets, which can have exposed to a higher stress concentration since the remaining cross section could no longer sustain the shear overload. The heavily deformed Al sheet eventually allowed the cracks to grow in the transverse direction, thus experienced the through-thickness crack growth. Similar results have been reported by Patel *et al.* [6] and Macwan and Chen [18].

3.6 Lap shear tensile fractography

Typical SEM images of tensile lap shear fracture surfaces of dissimilar USWed Al-to-AISI 304 stainless steel joint at a welding energy of 750 J and Al-to-ASTM A36 steel joint at a welding energy of 1500 J are shown in Fig. 13 and Fig. 14. As from the overall fracture surface of both joints (Fig. 13(a), (b) and Fig. 14(a), (b)), squeeze-out effect of materials at the edge of the nugget can be observed which was caused by the localized melting due to the high temperature and clamping pressure during the USW. However, as compared to Al-to-ASTM A36 steel joint in higher welding energy (i.e., 1500 J), more materials have been squeeze-out from Al-to-AISI 304 stainless steel joint at lower energy (i.e., 750 J).

To better understand the tensile fracture behavior of both joints, different regions (Al-Fe IMCs containing regions) were magnified. As seen from Fig. 13(c) and (e), most of the Al-Fe IMCs were found on the Al side as compared to the matching steel side as shown in Fig. 13(d) and (f) for Al-to-AISI 304 stainless steel joint. From the chemical composition analysis of Al-to-ASTM A36 steel joints, it can be observed that both the matching sides have Al-Fe IMCs containing regions as shown in Fig. 14(c), (e), (d), and (f). To further verify chemical compositions on the fracture surfaces, EDS point analysis of Al-to-AISI 304 stainless steel joint in the region A (the upper left corner of Fig. 13(c)) showed a composition of (in at.%) 61.8% Al, 27.6% Fe and 6.5% Cr equivalent to the θ ($FeAl_3$) phase, which was in good agreement with the XRD results shown in Fig. 5(a). Equivalent compositions have also been identified in the region D (the center of the weld nugget) as shown in Fig. 13(d) for matching steel side. Other region of both Al and steel sides exhibits more or less similar composition. On the other hand, EDS point analysis in the region A (the center of the weld nugget as shown in Fig. 14(c)) showed a composition of (in at.%) 75.1%Fe and 24.9%Al equivalent to the Fe_3Al phase, which is corroborated well with the XRD results shown in Fig. 5(b) as well. Other region of Al-to-ASTM A36 steel joints also showed equivalent compositions (Fig. 14(d), (e), and (f)). As seen from Fig. 14(c) to (f), the main difference between two joints could clearly be identified by observing the lack of higher aluminum-containing θ ($FeAl_3$) phase in ASTM A36 welded joints, as also reported in the study of dissimilar defocused laser beam lap welding of A6111-T4-to-cold-rolled steel plates (SPCC) by by Lee *et al.* [46].

4. Conclusions

High-power USW was used to join dissimilar aluminum to two commercial steel sheets at different levels of welding energy, and tensile lap shear tests were performed to determine the failure load and failure energy. The following conclusions could be drawn:

1. Microstructure observation revealed that θ ($FeAl_3$) phase was mainly present at the weld interface for both dissimilar joints in addition to η (Fe_2Al_5) phase in the Al-to-AISI 304 stainless steel joints and Fe_3Al phase in the Al-to-ASTM A36 steel joints.
2. AISI 304 stainless steel welds showed a higher hardness value as compared to the ASTM A36 steel welds due to the solid solution strengthening of Cr and high strength of the bulk AISI 304 stainless steel.
3. The average peak welding strength of Al-to-AISI 304 stainless steel weld samples was slightly higher than Al-to-ASTM A36 steel weld samples, whereas the fracture energies of Al-to-AISI 304 stainless steel weld samples were significantly higher as compared with Al-to-ASTM A36 steel weld samples. In general, the welding strength of both Al-to-AISI 304 stainless steel and Al-to-ASTM A36 steel weld samples were higher than other dissimilar USW joints reported in open literature.
4. Regardless the rapid weld cycle and solid-state nature of the USW process, the fracture surfaces exhibit that the IMC layer grows with increasing welding energy or time, whose inherent brittleness compromises the integrity of the joint.
5. The lap shear tensile fracture occurred from the Al/Fe interface in the case of lower energy inputs, the failure mode at higher welding energy inputs became the transverse through-thickness crack growth, which occurred at the edge of the nugget zone on the softer Al side.

Acknowledgements

The authors would like to thank the Natural Sciences and Engineering Research Council of Canada (NSERC) and Rio Tinto Aluminum, through the NSERC Industrial Research Chair in Metallurgy of Aluminum Transformation at the University of Québec at Chicoutimi (UQAC) for providing financial support. One of the authors (D.L. Chen) is grateful for the financial support by the Premier's Research Excellence Award (PREA), NSERC-Discovery Accelerator Supplement (DAS) Award, Canada Foundation for Innovation (CFI) and Ryerson Research Chair (RRC) program. The authors would also like to thank Messrs. A. Machin and Q. Li (Ryerson University) and Messrs. Dany Racine, Emelie Brideau, and Pier-Luc Privé (UQAC) for easy access to the laboratory facilities and their assistance in the experiments.

References

[1] McNutt M. The beyond-two-degree inferno. Science 2015;349:7.

[2] Chu S, Majumdar A. Opportunities and challenges for a sustainable energy future. Nature 2012;488:294-303.

[3] Creutzig F, Jochem P, Edelenbosch OY, et al. Transport: A roadblock to climate change mitigation? Science 2015;350:911-12.

[4] Ash C, Culotta E, Fahrenkamp-Uppenbrink J, et al. Once and future climate change. Science 2013;341:473.

[5] Schaedler TA, Jacobsen AJ, Carter WB. Toward lighter, stiffer materials. Science 2013;341:1181-82.

[6] Patel VK, Bhole SD, Chen DL. Ultrasonic spot welding of aluminum to high-strength low-alloy steel: microstructure, tensile and fatigue properties. Metall Mater Trans A 2014;45:2055-66.

[7] Wagner G, Balle F, Eifler D. Ultrasonic welding of hybrid joints. JOM 2012;64(3):401-6.

[8] Prangnell PB, Haddadi F, Chen YC. Ultrasonic spot welding aluminum to steel for automotive applications-microstructure and optimization. Mater Sci Tech 2011;27:617-24.

[9] Xiao L, Liu L, Zhou Y, Esmaeili S. Resistance-spot-welded AZ31 magnesium alloys: Part I. Dependence of fusion zone microstructures on second-phase particles. Metall Mater Trans A 2010;41(6):1511-22.

[10] Gallego-Juárez JA. Power ultrasonic: Applications of High-intensity Ultrasound. Oxford: Woodhead Publ.; 2015.

[11] Bakavos D, Prangnell PB. Effect of reduced or zero pin length and anvil insulation on friction stir spot welding thin gauge 6111 automotive sheet. Sci Technol Weld Join 2009;14(5):443-56.

[12] Liyanage T, Kilbourne J, Gerlich AP, North TH. Joint formation in dissimilar Al alloy/steel and Mg alloy/steel friction stir spot welds. Sci Technol Weld Join 2009;14(6):500-8.

[13] Prangnell PB, Bakavos D. Novel approaches to friction spot welding thin aluminium automotive sheet. Mat Sci Forum 2010;638-642:1237-42.

[14] Zhang CY, Chen DL, Luo AA. Joining 5754 automotive aluminum alloy 2-mm-thick sheets using ultrasonic spot welding. Weld J 2014;93:131s-138s.

[15] Patel VK, Bhole SD, Chen DL. Microstructure and mechanical properties of dissimilar welded Mg-Al joints by ultrasonic spot welding technique. Sci Technol Weld Join 2012;17(3):202-6.

[16] Mirza FA, Macwan A, Bhole SD, Chen DL. Ultrasonic spot welding of aluminum 5754 alloy: microstructure, tensile and fatigue properties. JOM 2016, accepted.

[17] Macwan A, Jiang XQ, Chen DL. Interfacial characterization of dissimilar joints between Al/Mg/Al-tri layered clad sheet to high-strength low-alloy steel. JOM 2015;67:1468-77.

[18] Macwan A, Chen DL. Ultrasonic spot welding of a rare-earth containing ZEK100 magnesium alloy: Effect of welding energy. Metall Mater Trans A 2016;47(4):1686-97.

[19] Bakavos D, Prangnell PB. Mechanisms of joint and microstructure formation in high power ultrasonic spot welding 6111 aluminum automotive sheet. Mater Sci Eng A 2010;527:6320-34.

[20] Gencsoy HT, Admas JA, Shigeo S. On some fundamental problems in ultrasonic welding of dissimilar metals. Weld J 1967;4:145s-153s.

[21] Esser G, Mys I, Schmidt MH. Laser micro welding of copper and aluminium using filler materials, Fifth International Symposium on Laser Precision Microfabrication, 2004;337-342.

[22] Annoni M, Carboni M. Ultrasonic metal welding of AA6022-T4 lap joints: Part I - Technological characterization and mechanical behavior. Sci Technol Weld Join 2011;16(2):107-15.

[23] Shakil M, Tariq NH, Ahmad M, et al. Effect of ultrasonic welding parameters on microstructure and mechanical properties of dissimilar joints. Mater Des 2014;55:263-73.

[24] Haddadi F, Strong D, Prangnell PB. Effect of Zinc coatings on joint properties and interfacial reactions in aluminum to steel ultrasonic spot welding. JOM 2012;64(3):407-13.

[25] Matsuoka SI, Imai H. Direct welding of different metals using ultrasonic vibration. J Mater Proc Technol 2009;209:954-60.

[26] Torkamany MJ, Sabbaghzadeh J, Hamedi MJ. Effect of laser welding mode on the microstructure and mechanical performance of dissimilar laser spot welds between low carbon and austenitic stainless steels. Mater Des 2012;34:666-72.

[27] Watanabe T, Sakuyama H, Yanagisawa A. Ultrasonic welding between mild steel sheet and Al-Mg alloy sheet. J Mater Process Technol 2009;209:5475-80.

[28] Sun YF, Fujii H, Takaki N, Okitsu Y. Microstructure and mechanical properties of dissimilar Al alloy/steel joints prepared by a flat spot friction stir welding technique. Mater Des 2013;47:350-7.

[29] Liu L, Xiao L, Chen DL, et al. Microstructure and fatigue properties of Mg-to-steel dissimilar resistance spot welds. Mater Des 2013;45:336-42.

[30] Bozzi S, Helbert-Etter AL, Baudin T, Criqui B, Kerbiguet JG. Intermetallic compounds in Al 6016/IF-steel friction stir spot welds. Mater Sci Eng A 2010;527:4505-9.

[31] Naoi D, Kajihara M. Growth behavior of Fe2Al5 during reactive diffusion between Fe and Al at solid-state temperatures. Mater Sci Eng A 2007;459:375-82.

[32] Chen S, Huang J, Ma K, Zhang H, Zhao X. Influence of a Ni-foil interlayer on Fe/Al dissimilar joint by laser penetration welding. Mater Lett 2012;79:296-9.

[33] Springer H, Kostka A, dos Santos JF, Raabe D. Influence of intermetallic phases and Kirkendall-porosity on the mechanical properties of joints between steel and aluminum alloys. Mater Sci Eng A 2011;528:4630-42.

[34] Chen YC, Bakavos D, Gholinia A, Prangnel PB. HAZ development and accelerated post-weld natural ageing in ultrasonic spot welding aluminum 6111-T4 automotive sheet. Acta Mater 2012;60:2816-28.

[35] Xu L, Wang L, Chen Y-C, Robson JD, Prangnell PB. Effect of interfacial reaction on the mechanical performance of steel to aluminum dissimilar ultrasonic spot welds. Metall Mater Trans A 2016;47A:334-46.

[36] Tsujino J, Hidai K, Hasegawa A, et al. Ultrasonic butt welding of aluminum, aluminum alloy and stainless steel plate specimens. Ultrasonics 2002;40:371-74.

[37] Rana R, Lahaye C, Ray RK. Overview of lightweight ferrous materials: strategies and promises. JOM 2014;66:1734-46.

[38] Lilly AC, Deevi SC, Gibbs ZP. Electrical properties of iron aluminides. Mater Sci Eng A 1998;258:42-49.

[39] Lee CY, Choi DH, Yeon YM, Jung SB. Dissimilar friction stir spot welding of low carbon steel and Al-Mg alloy by formation of IMCs. Sci Technol Weld Join 2009;14(3):216-20.

[40] Watanabe M, Feng K, Nakamura Y, Kumai S. Growth manner of intermetallic compound layer produced at welding interface of friction stir spot welded aluminum/steel lap joint. Mater Trans 2011;52(5):953-59.

[41] Chen YC, Nakata K. Effect of the surface state of steel on the microstructure and mechanical properties of dissimilar metal lap joints of aluminum and steel by friction stir welding. Metall Mater Trans A 2008;39A:1985-92.

[42] Shi H, Qiao S, Qiu R, Zhang X, Yu H. Effect of welding time on the joining phenomena of diffusion welded joint between aluminum alloy and stainless steel. Mater Manu Proc 2012;27(12):1366-69.

[43] Haddadi F. Rapid intermetallic growth under high strain rate deformation during high power ultrasonic spot welding of aluminium to steel. Mater Des 2015;66:459-72.

[44] Qiu R, Shi H, Zhang K, et al. Interfacial characterization of joint between mild steel and aluminum alloy welded by resistance spot welding. Mater Charact 2010;61:684-8.

[45] Qiu R, Zhang X, Hongxin, Yu H, Zhang K. Interfacial characterization of joint between mild steel and aluminum alloy welded by resistance spot welding. Adv Mater Res 2011;230-232:982-6.

[46] Lee K-J, Kumai S, Arai T. Interfacial microstructure and strength of steel to aluminum alloy lap joints welded by a defocused laser beam. Mater Trans 2005;46(8):1847-56.

[47] Liu K, Cao X, Chen X-G. A new iron-rich intermetallic-AlmFe phase in Al-4.6Cu-0.5Fe cast alloy. Metall Mater Trans A 2012;43A:1097-101.

[48] Liu K, Cao X, Chen X-G. Solid-state transformation of iron-rich intermetallic phases in Al-Cu 206 cast alloys during solution heat treatment. Metall Mater Trans A 2013;44A:3494-503.

[49] Jahn R, Cooper R, Wilkosz D. The effect of anvil geometry and welding energy of microstructures in ultrasonic spot welds of AA6111-T4. Metall Mater Trans A 2007;38A:570-83.

[50] Patel VK, Bhole SD, Chen DL. Improving weld strength of magnesium to aluminum dissimilar joints via tin interlayer during ultrasonic spot welding. Sci Technol Weld Join 2012;17(5):342-7.

[51] Fukumoto M, Miyagawa K, Tsubaki M, Yasui T. Spot welding between aluminum alloy and steel by friction stirring. Mater Sci Forum 2010;638-642:1227-32.

[52] Macwan A, Chen DL. Microstructure and mechanical properties of ultrasonic spot welded copper-to-magnesium alloy joints. Mater Des 2015;84:261-9.

[53] Macwan A, Chen DL. Ultrasonic spot welding of rare-earth containing ZEK100 magnesium alloy to 5754 aluminum alloy. Mater Sci Eng A 2016;666:139-48.

Table 1 Nominal chemical composition (wt.%) of the materials.

Material	Chemical composition (wt.%)										
	Mn	Si	Cu	Ni	Cr	Mg	C	S	P	Fe	Al
6061-T6	0.07	0.71	0.3	–	0.14	1.14	–	–	–	0.18	Bal.
AISI 304	0.98	0.62	–	8.05	18.21	–	0.05	0.004	0.028	Bal.	–
ASTM A36	0.80	0.40	0.2	–	–	–	0.25	0.050	0.040	Bal.	–

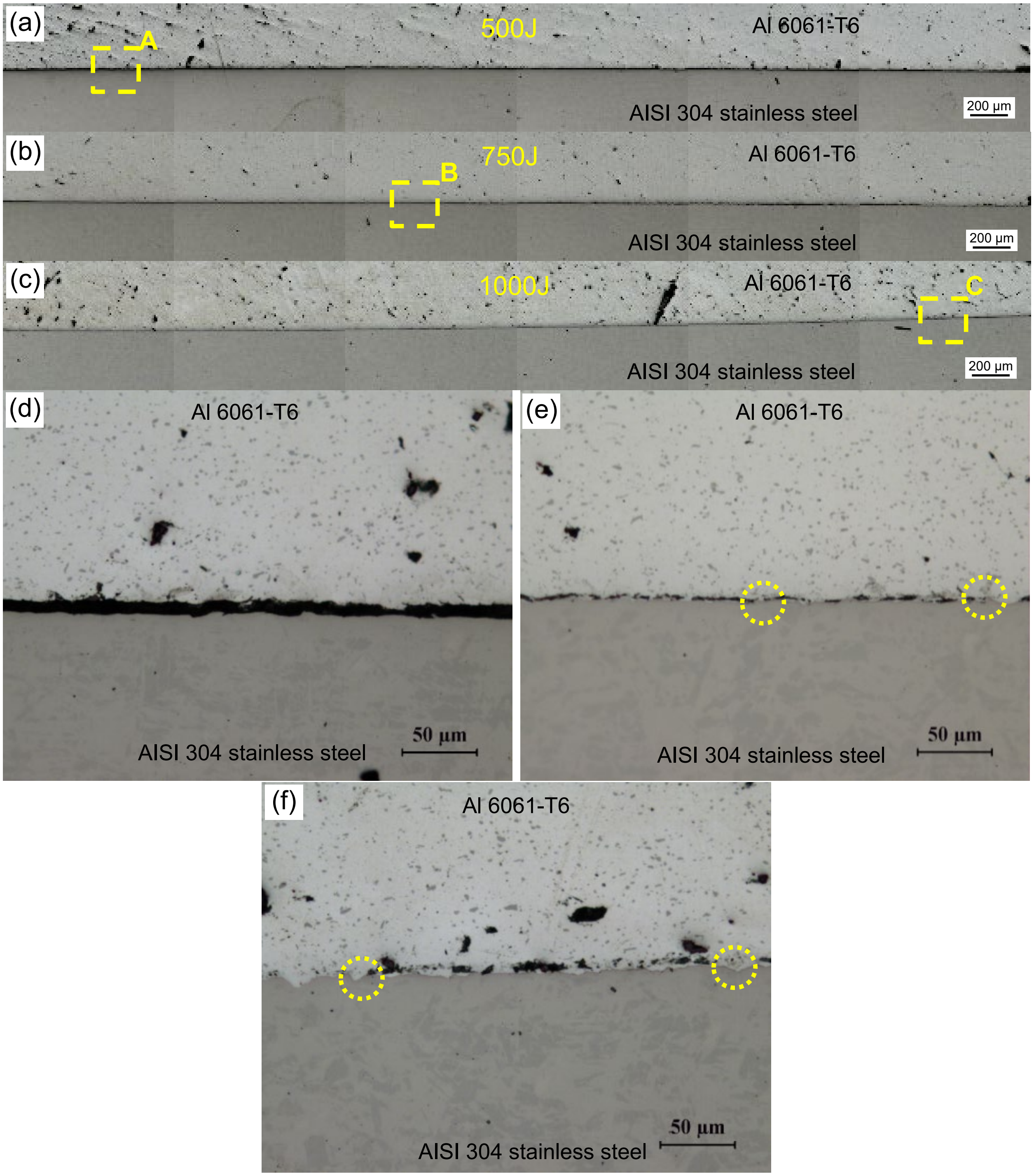

Fig. 1 Typical optical micrographs of a dissimilar USWed Al 6061-T6-to-AISI 304 stainless steel alloy cross-section ((a), (b), and (c)) overall view at a welding energy level of 500 J, 750 J, and 1000 J, respectively, and ((d), (e), and (f)) higher magnification images of region A, B, and C, in (a), (b), and (c), respectively.

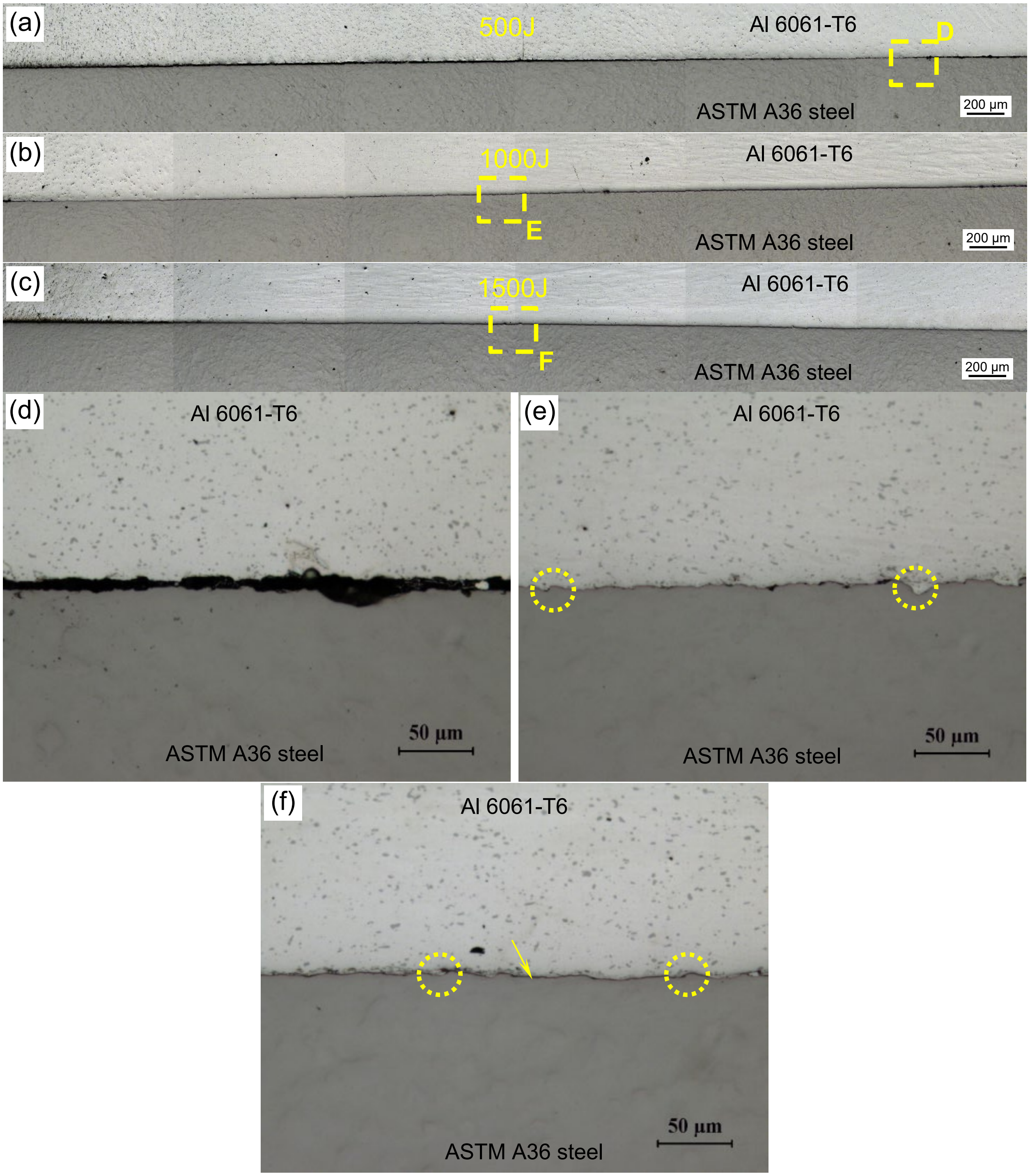

Fig. 2 Typical optical micrographs of a dissimilar USWed Al 6061-T6-to-ASTM A36 steel alloy cross-section ((a), (b), and (c)) overall view at a welding energy level of 500 J, 1000 J, and 1500 J, respectively, and ((d), (e), and (f)) higher magnification images of region D, E, and F, in (a), (b), and (c), respectively.

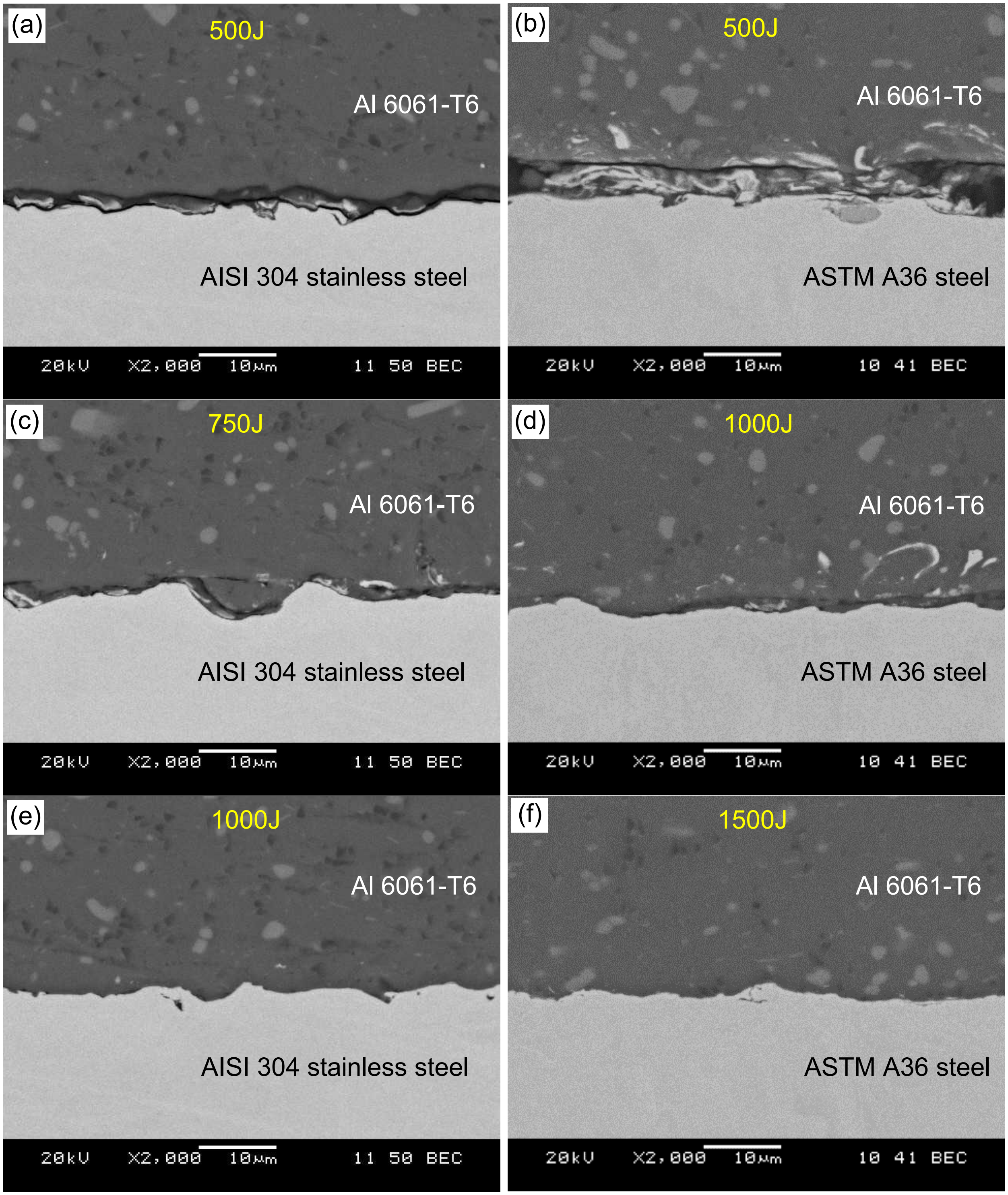

Fig. 3 SEM back-scattered electron images at the interface of the dissimilar USWed Al 6061-T6-to-AISI 304 stainless steel alloy ((a), (c), and (e)) and dissimilar USWed Al 6061-T6-to-ASTM A36 steel alloy ((b), (d), and (f)) at different energy inputs.

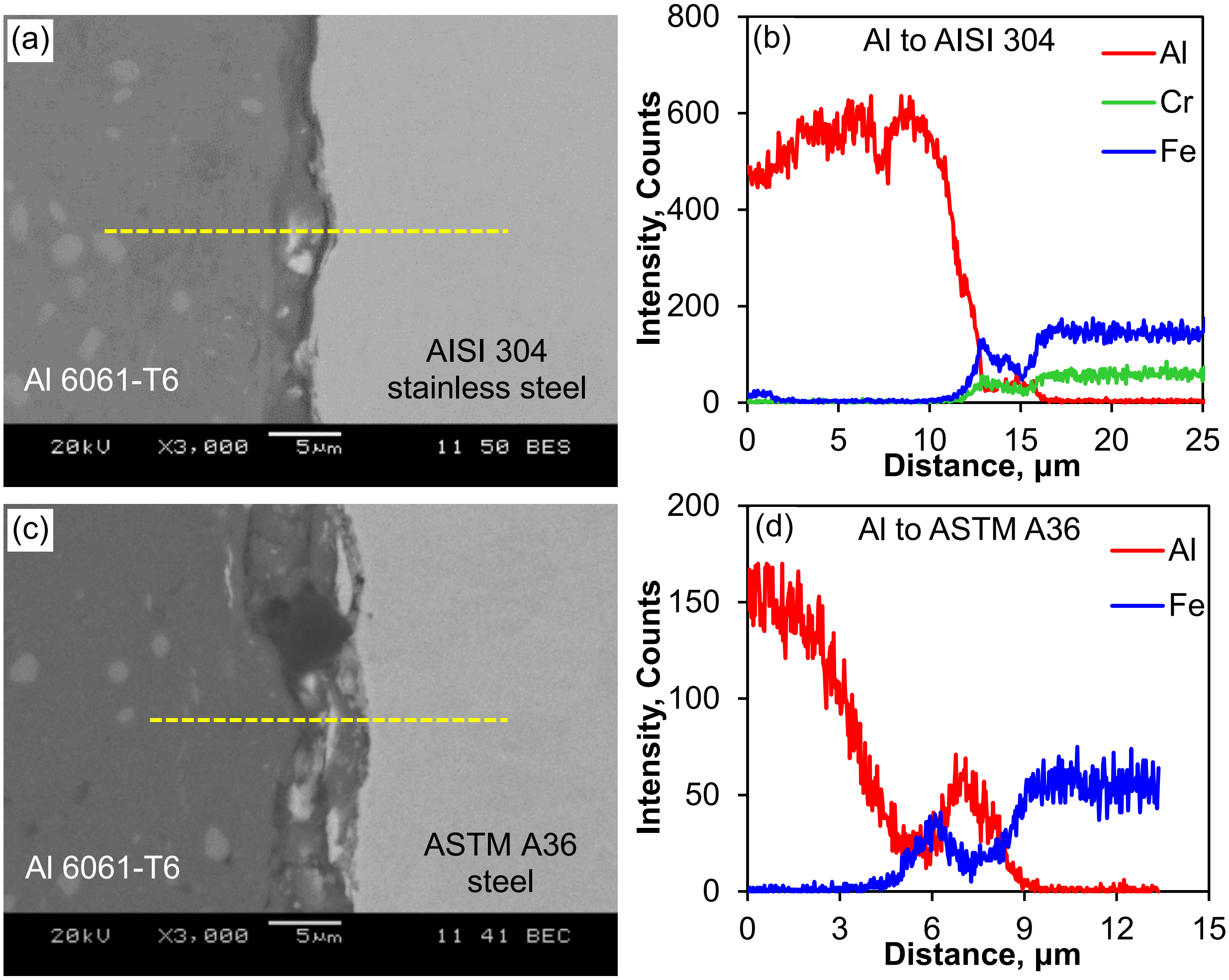

Fig. 4 SEM back-scattered electron images with EDS line scan positions and the corresponding EDS results at the interface of dissimilar USWed Al 6061-T6-to-AISI 304 stainless steel ((a) and (b)) and Al 6061-T6-to-ASTM A36 steel joints ((c) and (d)) at a welding energy of 500 J.

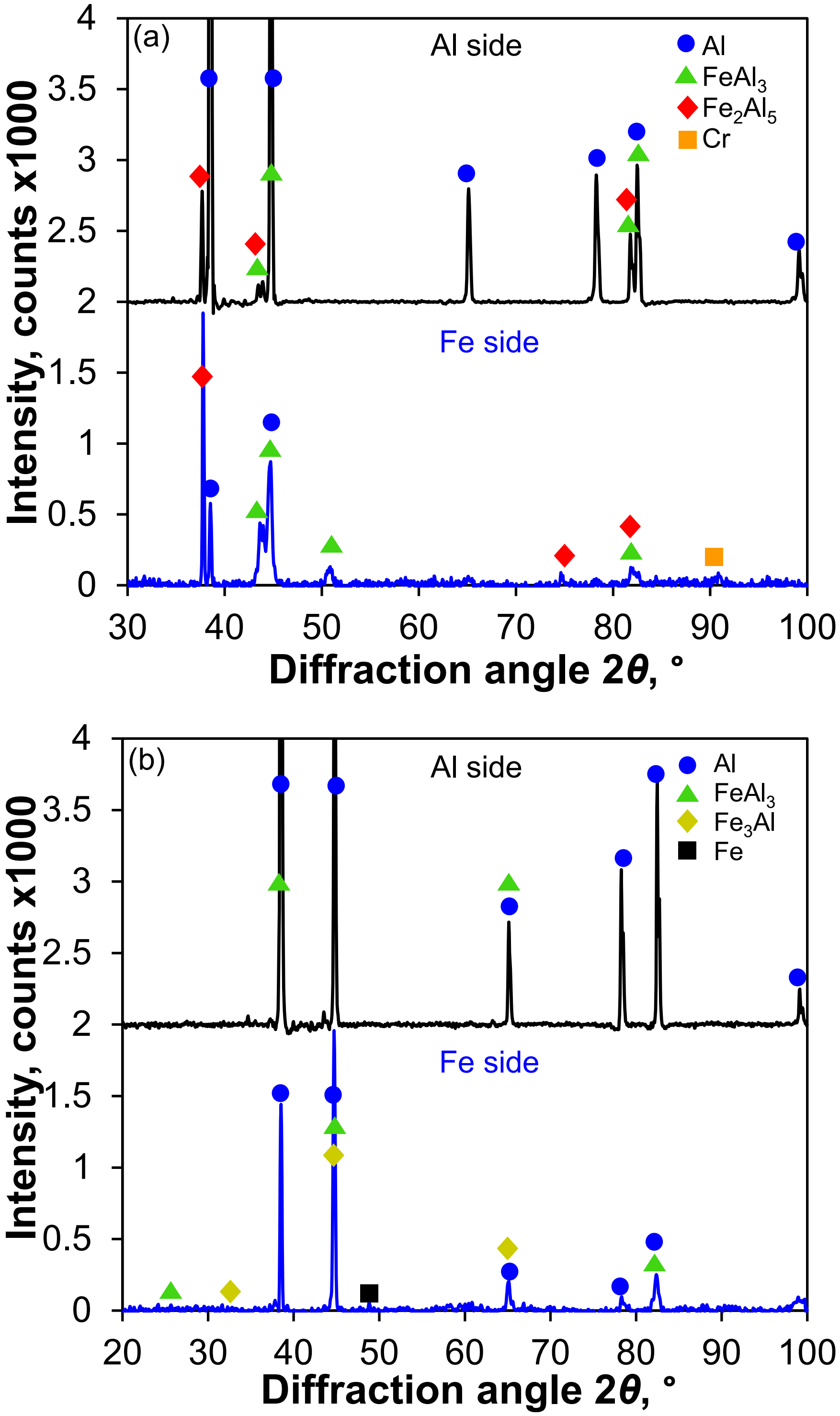

Fig. 5 XRD patterns obtained from the matching fracture surfaces of dissimilar USWed Al 6061-T6-to-AISI 304 stainless steel alloy joints (a) at a welding energy of 750 J and Al 6061-T6-to-ASTM A36 steel alloy joints (b) at a welding energy of 1500 J.

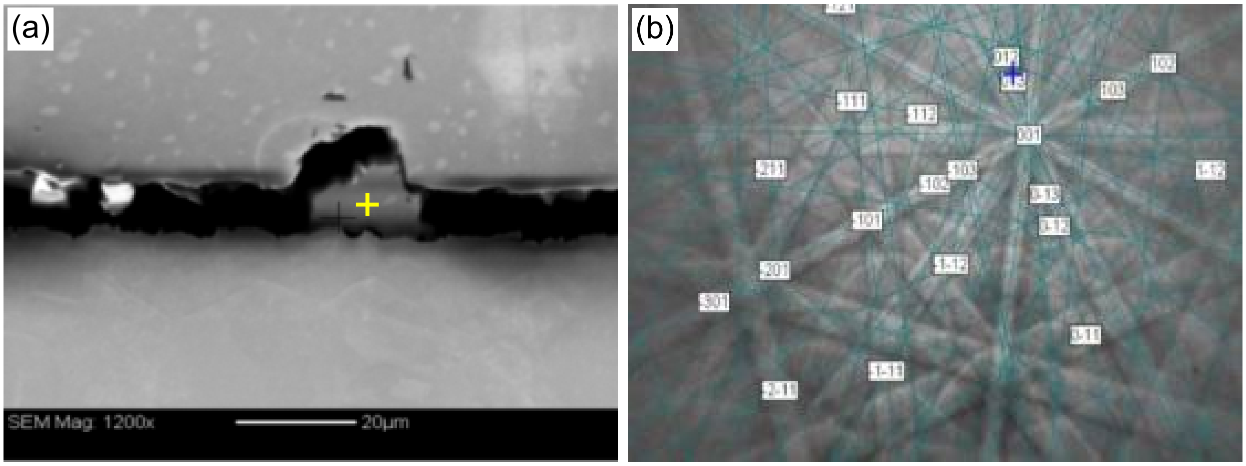

Fig. 6 Phase morphology and simulation results (indexed Kikuchi pattern) for the $FeAl_3$ phase in a dissimilar USWed Al 6061-T6-to-AISI 304 stainless steel joint at a welding energy of 500 J (MAD = 0.464).

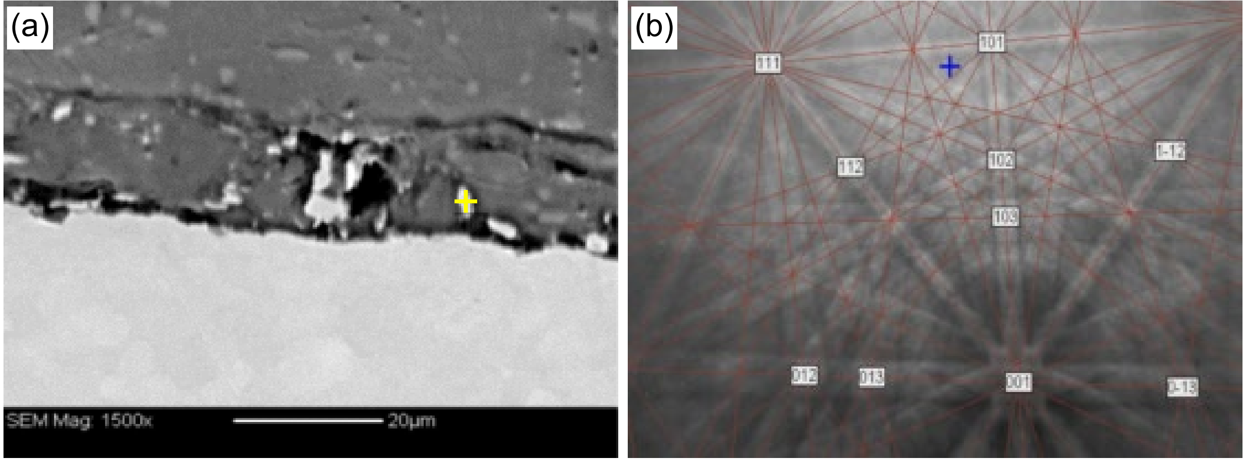

Fig. 7 Phase morphology and simulation results (indexed Kikuchi pattern) for the Fe_3Al phase in a dissimilar USWed Al 6061-T6-to-ASTM A36 steel joint at a welding energy of 500 J (MAD = 0.634).

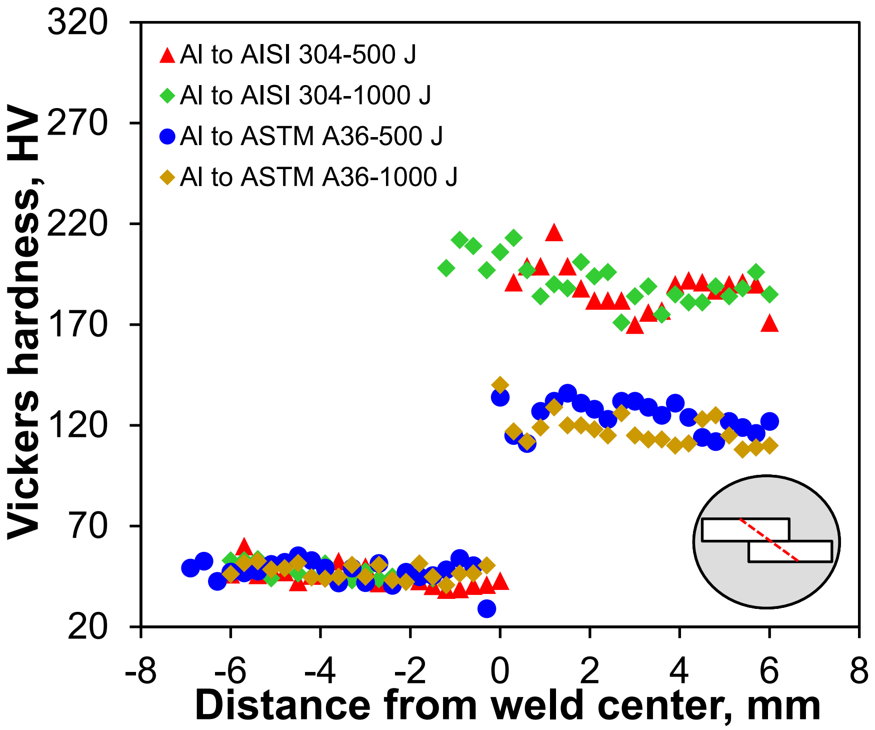

Fig. 8 Microhardness profiles across the interface of dissimilar USWed Al 6061-T6-to-AISI 304 stainless steel (a) and Al 6061-T6-to-ASTM A36 steel (b) joints at different welding energy inputs.

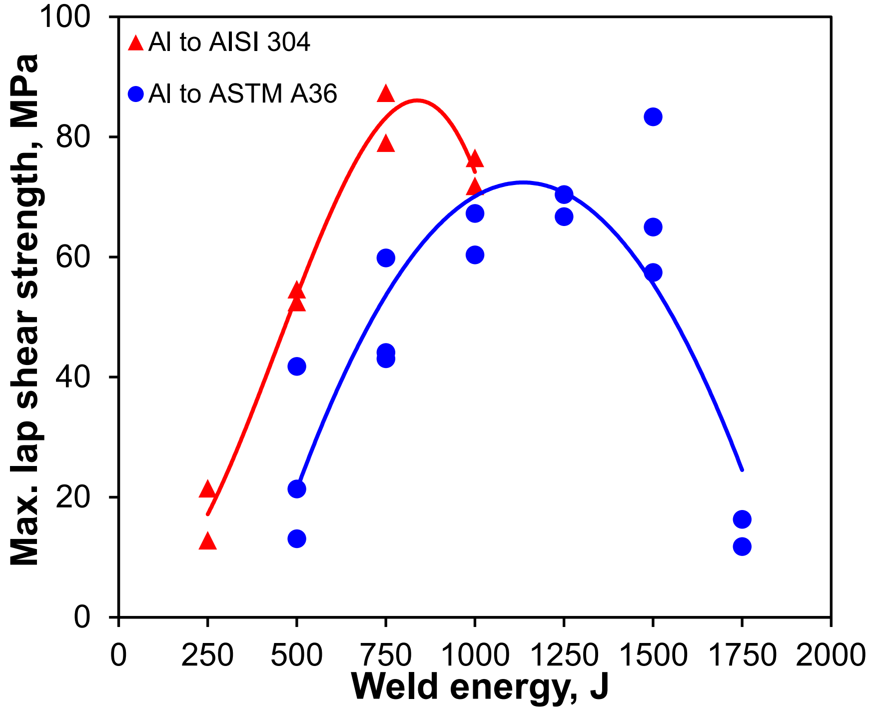

Fig. 9 Maximum tensile lap shear strength of dissimilar USWed Al 6061-T6-to-AISI 304 stainless steel (a) and Al 6061-T6-to-ASTM A36 steel (b) joints at different energy inputs.

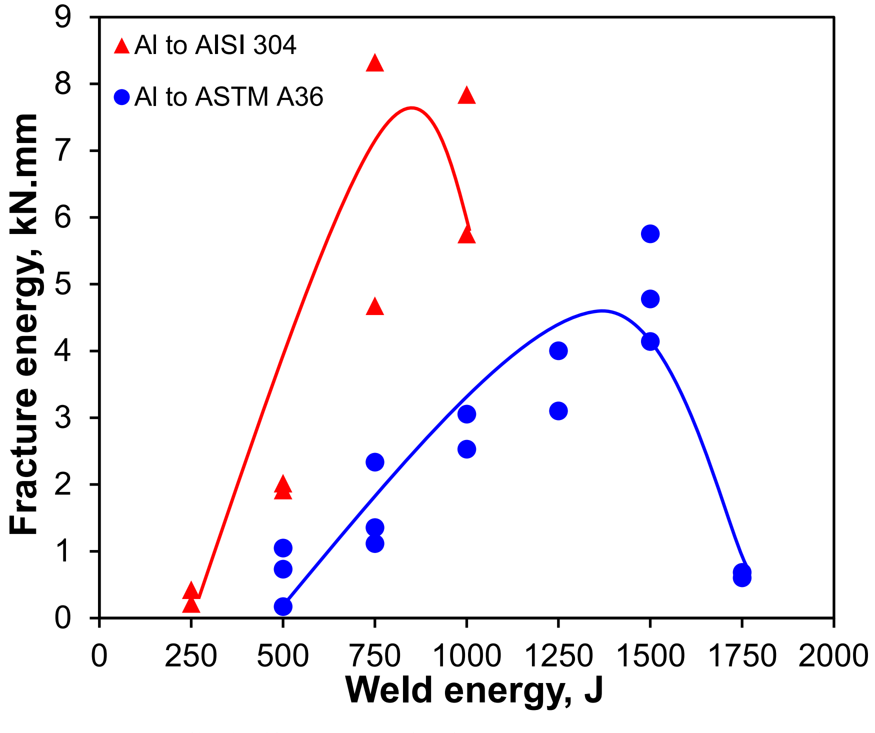

Fig. 10 Fracture energy of dissimilar USWed Al 6061-T6-to-AISI 304 stainless steel (a) and Al 6061-T6-to-ASTM A36 steel (b) joints at different energy inputs.

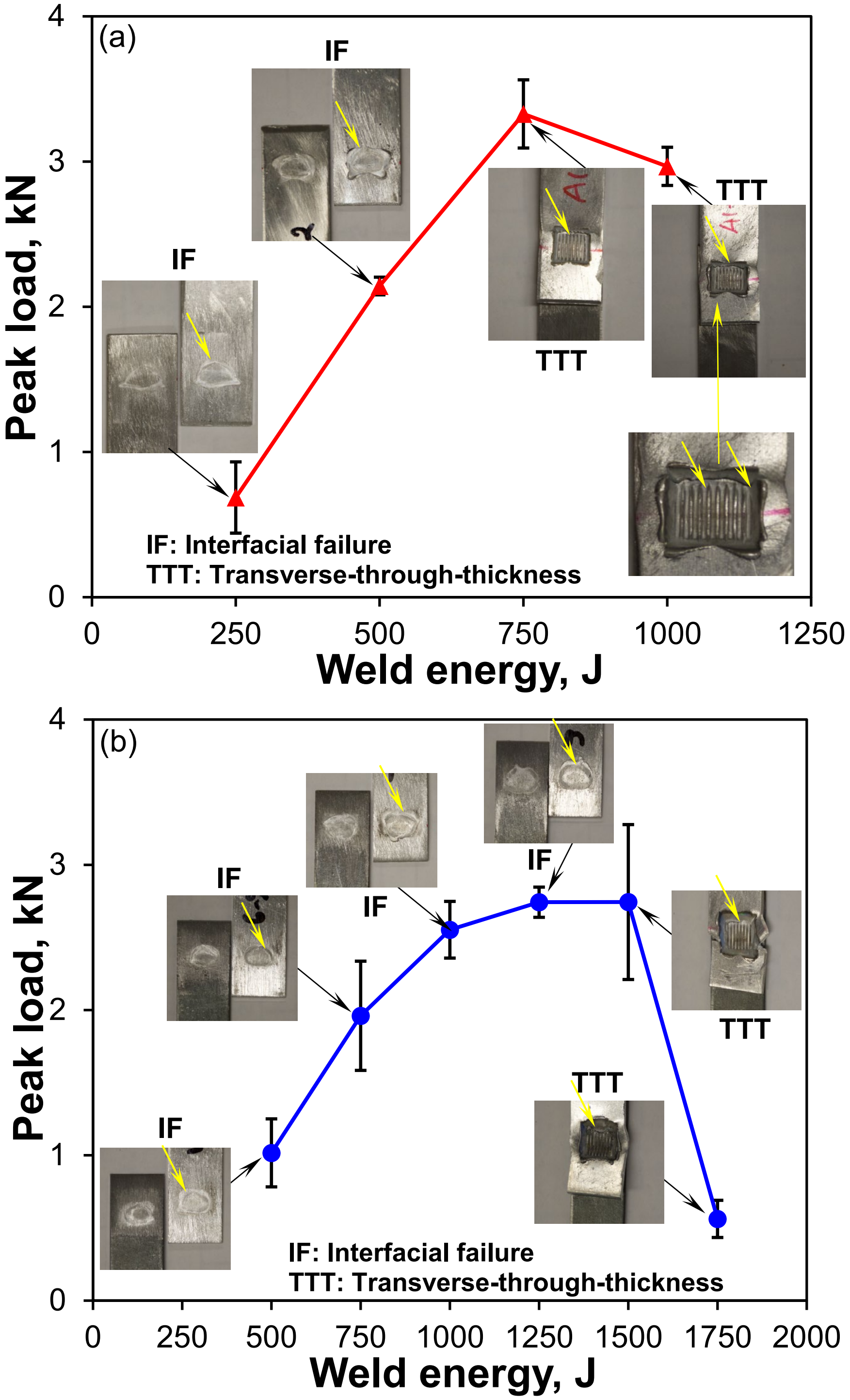

Fig. 11 Effect of welding energy on the tensile lap shear peak load of dissimilar USWed Al 6061-T6-to-AISI 304 stainless steel (a) and Al 6061-T6-to-ASTM A36 steel (b) joints along with typical failure modes and locations (indicated by yellow arrows).

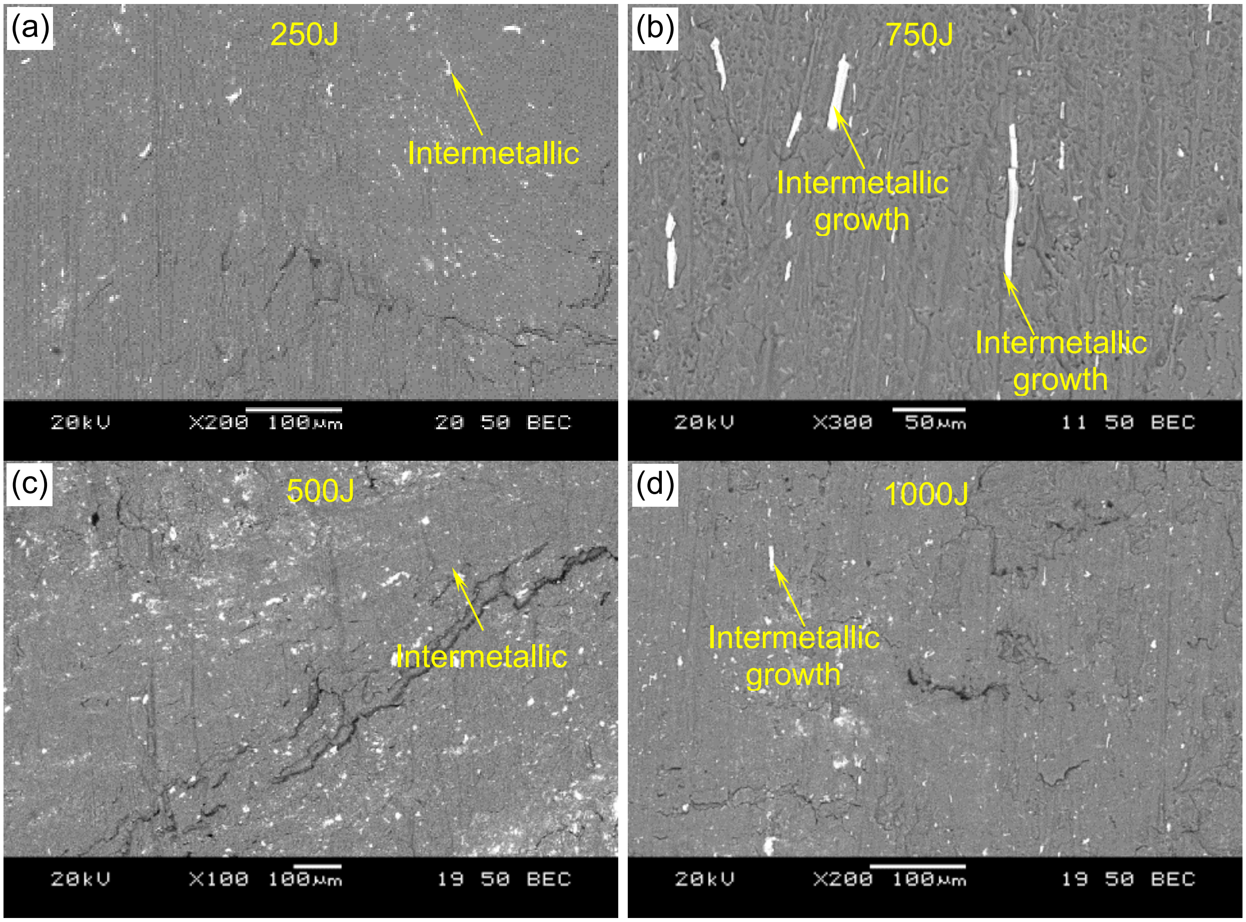

Fig. 12 Intermetallic growth on the Al side of dissimilar USWed Al 6061-T6-to-AISI 304 stainless steel joints ((a) and (b)) and Al 6061-T6-to-ASTM A36 steel joints ((c) and (d)) at different energy inputs.

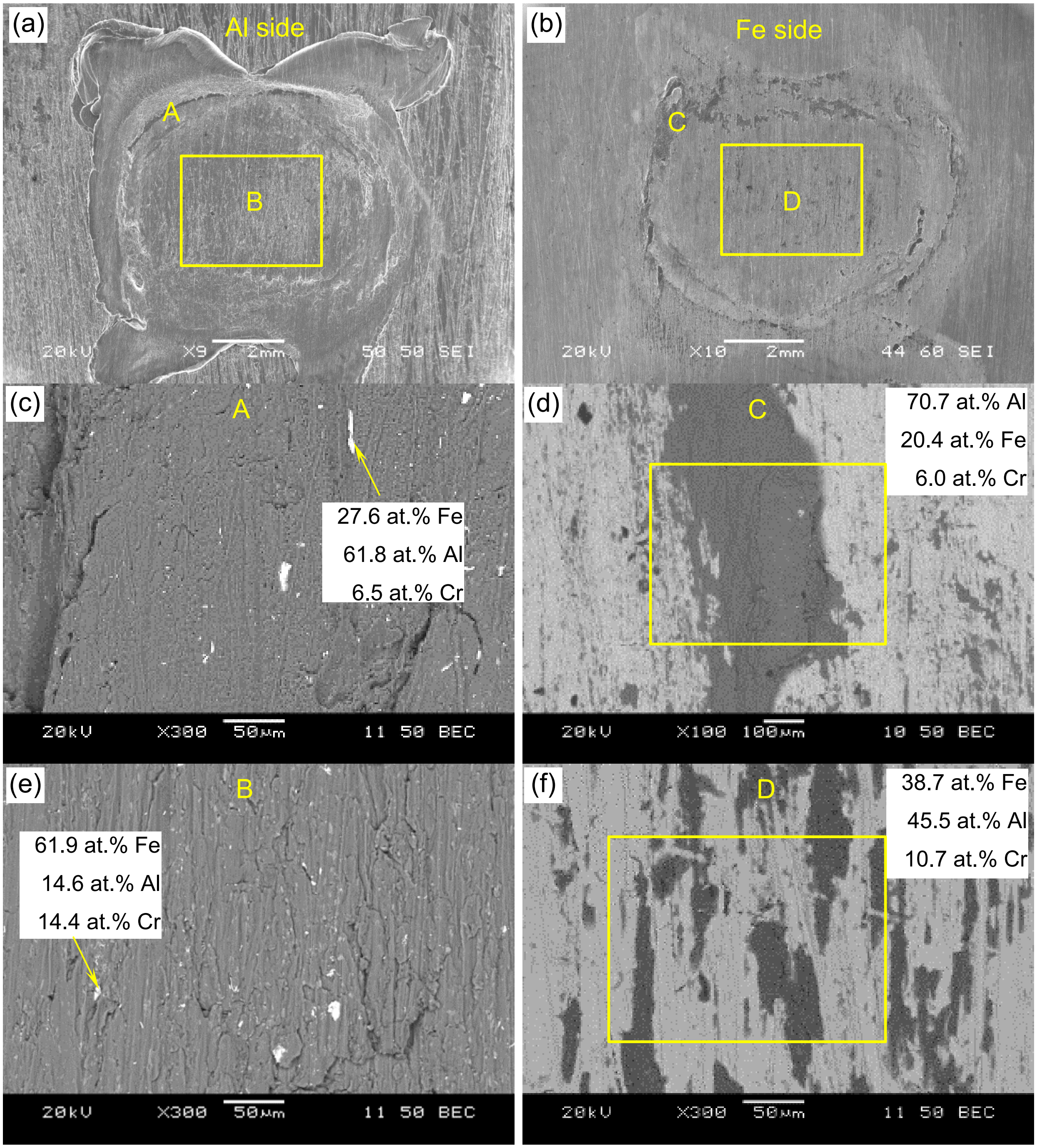

Fig. 13 Typical SEM back-scattered electron images of tensile lap shear fracture surface of a dissimilar USWed Al 6061-T6-to-AISI 304 stainless steel joint made at a welding energy of 750 J: (a) overall view of Al side, (b) overall view of Fe side, ((c) and (e)) higher magnification images of regions A and B, respectively, and ((d) and (f)) higher magnification images on regions C and D, respectively.

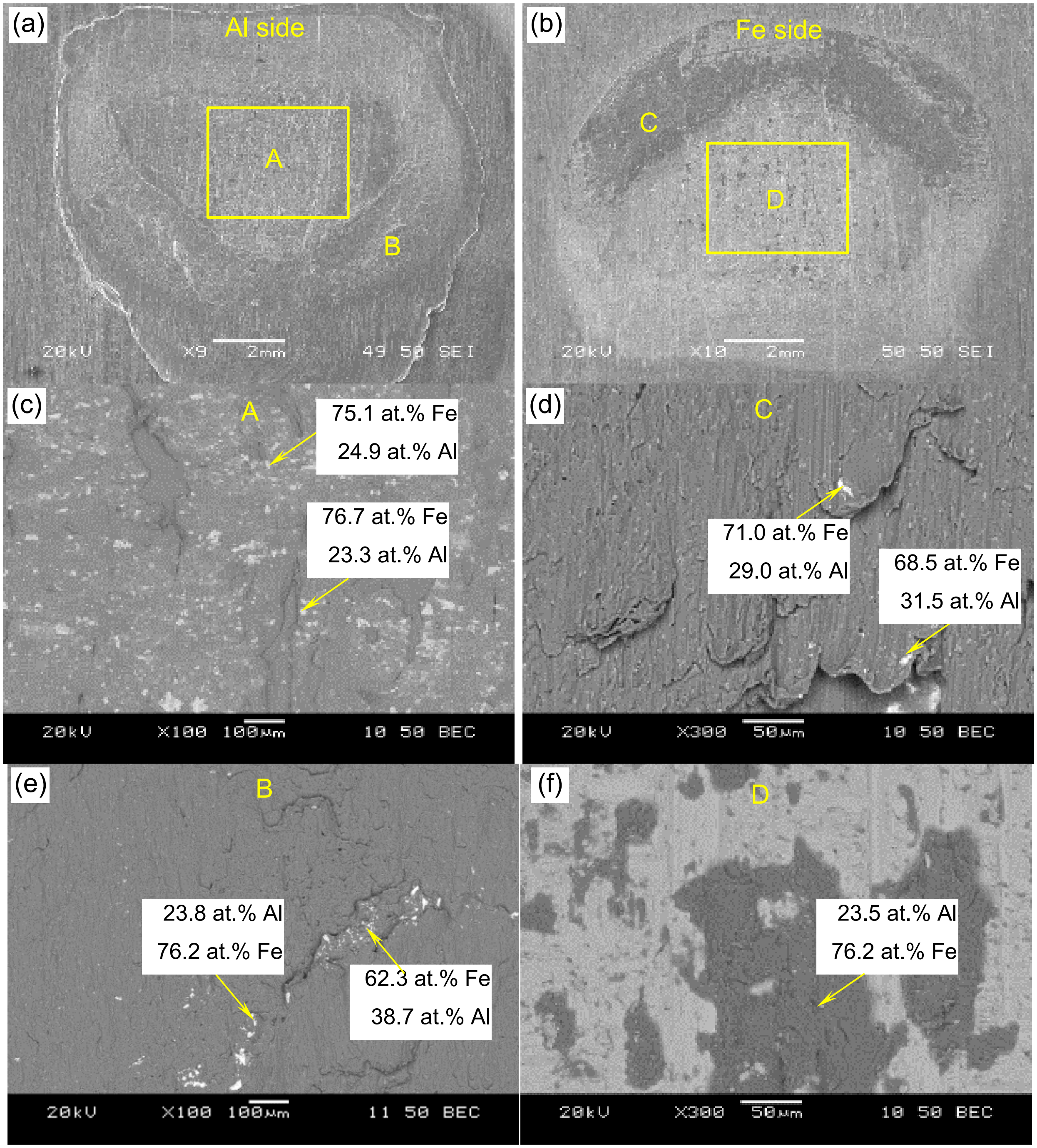

Fig. 14 Typical SEM back-scattered electron images of tensile lap shear fracture surface of a dissimilar USWed Al 6061-T6-to-ASTM A36 steel joint made at a welding energy of 1500 J: (a) overall view of Al side, (b) overall view of Fe side, ((c) and (e)) higher magnification images of regions A and B, respectively, and ((d) and (f)) higher magnification images on regions C and D, respectively.